

Effect of Streamwise Slots on the Drag of a Transonic Projectile

A. Ibrahim* and A. Filippone†

University of Manchester, Manchester, M60 1QD England, United Kingdom

DOI: 10.2514/1.30439

Streamwise slots have been applied to a projectile at transonic speeds as a passive method for controlling normal shock wave/turbulent boundary-layer interaction. The slots are cut on the cylindrical and boattail skins, where shock waves are formed. This study aimed to investigate the effects of the slots on the drag at Mach numbers ranging from 0.85 to 1.10. Investigation of the suction and blowing mechanism through the slots showed a trend similar to a porous surface applied to the area of flow control. This type of control transforms the normal shock wave into a weaker lambda shock structure. Moreover, it produces a thicker boundary-layer profile along and downstream of the slots compared to the baseline boundary layer of a solid wall. Investigation of the flow pattern at a Mach number of 0.96 shows two opposite streamwise circulation vortex pairs: a vortex over the slot surface on the blowing region, and another inside the cavity at the suction region. Finally, a single vortex normal to the freestream direction is formed inside the cavity in the blowing region.

Nomenclature

C_D	= total drag coefficient
C_{db}	= base drag coefficient
C_{dp}	= pressure drag coefficient
C_{dsf}	= skin friction drag coefficient
C_f	= form drag coefficient
c_p	= pressure coefficient
c_{pb}	= base pressure coefficient
D	= projectile caliber
M	= freestream Mach number
N	= number of cells
N_G	= number of cells for the used grid
r	= radius of projectile base
u	= axial velocity component
v_n	= velocity normal to the slot surface
y^+	= wall y^+ function
β	= boattail angle
δ	= boundary-layer thickness
θ	= azimuth angle

I. Introduction

DRAg reduction of artillery projectiles has always been an important issue in order to increase the ballistic range. The base drag has been recognized as a major part of the total drag. Thus, base drag reduction is an effective approach to get better ballistic performance [1]. Boattailing is the simplest method to reduce the base drag, although it has two unfavorable penalties at transonic speeds. The first is the generation of large Magnus forces and moments that adversely affect the gyroscopic and dynamic stability of the projectile [2]. The second penalty is due to the formation of a normal shock wave over the boattail which results in an increase in wave drag, especially with large boattail angles ($\beta > 5$ deg) [3]. This can be shown in Fig. 1 where the drag breakdown versus Mach

number is displayed at transonic speeds. It is noticed that the form drag is the dominant component in the transonic speed region with a maximum value at a Mach number of 0.96. The present results are in comparison with available results in [4] using thin-layer axisymmetric Navier–Stokes equations associated with the Baldwin–Lomax turbulence model. Both of the numerical results illustrate similar trend for the percentage of each drag component. Thus, a method of flow control technique is required to reduce the form drag.

There are two techniques for the control of shock wave/boundary-layer interaction (SBLI). The first is an active method which is not feasible in its application on projectiles as shown by Liang and Fu [5]. The second technique is the passive control which is achieved by using a recirculating cavity flow device. Among these devices is the arrangement of a porous surface with a cavity underneath which is considered as the conventional method. Experimental studies on an airfoil have been performed by Bahi et al. [6] and Nagamatsu et al. [7] showing the effect of applying porosity on an airfoil. These studies showed that a shock wave could be removed by applying an appropriate distribution of porosity on the upper wall of an airfoil. Further studies showed that porous surfaces on airfoils favorably affect the drag and lift forces [8–12]. This method has been applied to the boattail part of a projectile for the first time by Liang and Fu [3]. Their numerical study showed a wave drag reduction at transonic speeds. Thereafter, computational studies showed the effect of applying porous surfaces with and without splitters in the cavity on both cylindrical and boattail parts at different angles of attack [13,14]. The effect of porosity has been recently demonstrated by the authors through applying different porosity strengths to both the suction and the blowing regions [15].

Although applying porosity shows beneficial effects on wave drag reduction, some unfavorable effects on the viscous losses due to thickening of the boundary layer over the whole porous surface have been detected [16,17]. A novel method of SBLI control has been experimentally performed by Smith et al. on the upper surface of a two-dimensional transonic airfoil [18]. The results presented by Smith and his coauthors revealed a decrease in drag and an increase in lift by using slots on the upper surface of an airfoil. This method has limited effect on the viscous losses, where the thickening of the boundary layer is confined to the slot width. Thus, the present study deals with a secant-ogive-cylinder-boattail (SOCBT) projectile fitted with streamwise slots at transonic speeds. The purpose of the study is to investigate, with the available computational resources, the effect of streamwise slots on the total drag. Herein, the use of streamwise slots is applied for the first time to a projectile as an alternative method to the use of a conventional porous wall.

Received 13 February 2007; revision received 2 May 2007; accepted for publication 4 May 2007. Copyright © 2007 by A. Ibrahim and A. Filippone. Published by the American Institute of Aeronautics and Astronautics, Inc., with permission. Copies of this paper may be made for personal or internal use, on condition that the copier pay the \$10.00 per-copy fee to the Copyright Clearance Center, Inc., 222 Rosewood Drive, Danvers, MA 01923; include the code 0021-8669/07 \$10.00 in correspondence with the CCC.

*Post-Graduate Student, School of Mechanical, Aerospace, Civil Engineering.

†Lecturer, School of Mechanical, Aerospace, Civil Engineering, George Begg Building, P.O. Box 88; a.filippone@manchester.ac.uk. Senior Member AIAA (Corresponding Author).

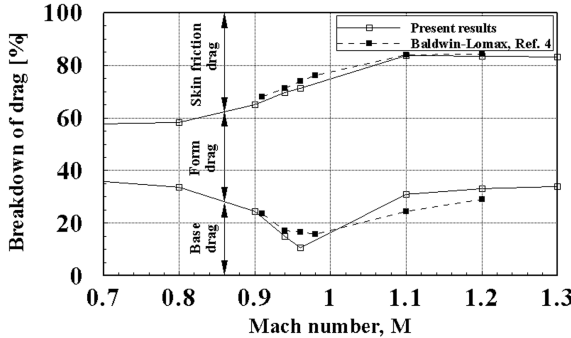


Fig. 1 Breakdown of drag components versus Mach number at transonic speeds.

II. Computational Method

The computational investigation in this study was carried out by applying the Reynolds-averaged Navier-Stokes equations (RANS) in time-independent form using the commercial code Fluent. The coupled-implicit scheme was used to solve the system of differential equations. The second-order upwind scheme was used in discretizing the spatial dependent properties in RANS equations. The Spalart-Allmaras [19] turbulence model was used in this study. This model was developed for aerodynamics applications and gave good results in the present case.

The relative dimensions in terms of projectile caliber D are shown in Fig. 2. The skins of cylindrical and boattail parts are cut by eight slots. The slots are homogeneously distributed around the circumference. Each slot has a 1.0 mm width. This is approximately equal to the boundary-layer momentum thickness at a station on the solid surface just upstream of the start of the cylindrical slots. A 4.0 mm cavity depth is underneath the 1.0 mm thick slots. The distance between two successive slots is approximately 0.4 D . This distance was chosen to give some relaxation of the boundary-layer thickness [20].

A. Grid Generation

Performing a robust and accurate computational fluid dynamics (CFD) calculation requires optimization between the grid size and its quality. On the one hand, the grid size should be minimized to get robust simulation. On the other hand, the grid quality should be taken into consideration to get an accurate and converged solution. A grid independent solution is the only way to achieve these two basic aspects. The key result that was monitored in the grid sensitivity study is the total drag coefficient.

1. Solid-Wall Projectile

To match its counterpart in the case of controlled SBLI, the domain around the solid projectile has been divided into eight sectors. Then, one sector was selected to be the computational domain. Figure 3 shows an overall view of the structured grid of hexahedron/wedge cells as well as a detailed view for the mesh over the cylindrical part. The structured grid is more economical in the present case because a much larger aspect ratio (up to 140 near the walls) than the tetrahedral cells can be used. To resolve the viscous

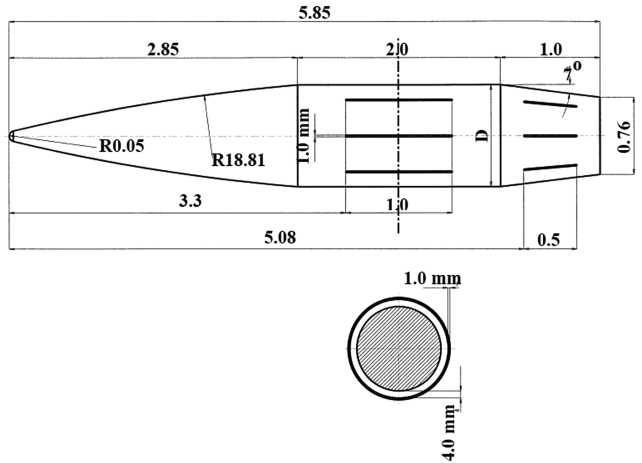


Fig. 2 Relative dimensions of SOCBT projectile.

sublayer, the height of the cells adjacent to the projectile surface has been taken equal to $3.5 \times 10^{-5} D$. The cells were stretched toward the pressure far field by a ratio equal to 1.24. The value of the wall function $y^+ < 1.0$ for the wall adjacent cells was checked to confirm the sufficient resolution of the mesh near the wall.

Five grids have been tested on the solid projectile at a Mach number of 0.96 to obtain the grid independent solution. The coarsest grid consists of 270,600 cells. Figure 4 shows the variation of the total drag coefficient with the grid size normalized by the number of cells for the used grid (N_G). The fourth grid is one for the solution independency because there is no significant change in the drag coefficient from grid 4 to grid 5. Thus, a mesh of 627,000 cells has been used with streamwise spacing $\Delta x < 0.3\delta$ at the region of SBLI, where δ is the boundary-layer thickness upstream of the position of interaction.

2. Slotted-Wall Projectile

Figure 5 shows the slotted-wall projectile model and the cavity-slot arrangements. Three main steps were followed to generate the mesh in the case of the slotted-wall projectile. The first step is the grid generation around the solid projectile. The second step is the grid generation in the cavity-slot arrangements using tetrahedron cells. The last step is merging both of the generated grids. The sensitivity study of the grid was performed at a Mach number of 0.96 because the form drag has a maximum value at this speed, as shown in Fig. 1. The initial size of the mesh was 675,000 cells. Although it is known a priori that a finer mesh is required in the region around the slot, this region has been refined until the solution showed a neglected change in the total drag coefficient. Three stages of region adaption of the grid have been performed. So, three coaxial cylindrical regions have been constructed around each slot. Each cell in the outer cylinder is divided into four cells in the intermediate cylinder. Then, the four cells in the intermediate cylinder will be 16 in the inner one (as shown in Fig. 6). Therefore, the number of cells on the slot opening is duplicated each time of region adaption to get 16 cells per the 1.0 mm slot width. After refinement of the grid around the slot, the final mesh size is approximately 1.8×10^6 cells.

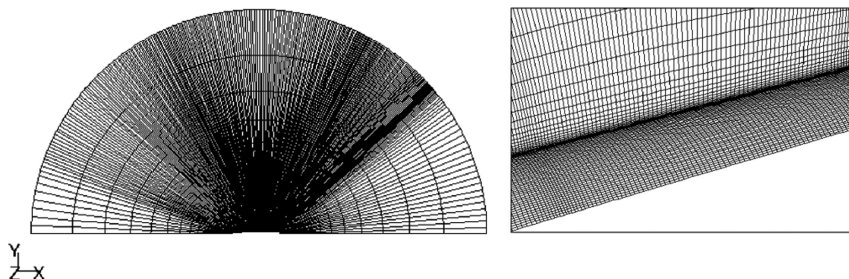


Fig. 3 Three-dimensional grid for the solid-wall projectile.

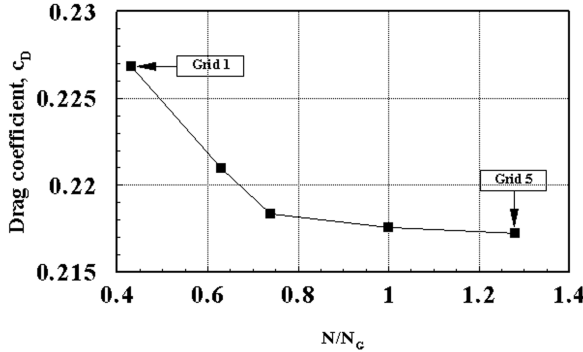


Fig. 4 Variation of the total drag coefficient for the tested grids at $M = 0.96$.

B. Boundary Conditions

Figure 7 displays the used boundary conditions which are the pressure far-field boundary on the uniform upstream flow at a distance equal to $23D$, the symmetric boundary on both sides of the computational domain, and the adiabatic no-slip conditions on the solid projectile wall and on the walls of the cavity-slot arrangements.

To construct a structured mesh, it was required to divide the computational domain into two main blocks. The first block is over the uncontrolled surfaces. The second block is over the controlled surfaces around both the cylindrical and the boattail parts. The two blocks were merged through the interface boundary condition to get the mesh in its final form.

III. Results and Discussions

A. Flow Over the Solid Projectile

A stagnation temperature of 320 K and a Reynolds number $Re = 4.5 \times 10^6$ based on the projectile length were used. The numerical experiments were performed at zero angle of attack. The flow past the solid projectile was simulated at Mach numbers equal to 0.85, 0.90, 0.96, and 1.10. The experimental data of the pressure coefficient past the solid projectile shown in [13] were chosen to validate the computational work. The nose of the present model was changed into part of a 3 mm radius sphere, instead of a sharp edge. The rounded nose improved the skewness of the cells on the projectile nose. It has been found that the change in geometry has a neglected effect on the flow along the projectile. Figure 8 shows a comparison between calculated and measured pressure coefficients on the solid projectile at a Mach number of 0.96. There is good

agreement between the present results and the measured data along the projectile body.

Figure 9 illustrates the development of the Mach contours around the solid-wall projectile at the transonic region. At Mach 0.85, the contours show clustering around the circumference of the projectile, where there are changes in the projectile geometry. This clustering is the formation of small supersonic domains. As the Mach number is increasing to 0.90, these domains enlarge, and an interaction between the shock waves and the viscous flow starts. At Mach 0.96, normal shock waves on the middle of both cylindrical and boattail parts are formed where SBLI occurs. At Mach 1.10, the normal shock waves are transformed into oblique ones.

Figure 10 shows the pressure coefficient distribution over both of the cylindrical and boattail parts at Mach numbers ranging from 0.85 to 1.10. It is noted that the adverse pressure gradient is maximum at Mach 0.96 for both of the cylindrical and boattail parts. This gives the indication that strong SBLI occurs at this Mach number. However, the pressure gradient at Mach numbers 0.85 and 0.90 is almost constant, except at the junctions between projectile parts. For the flow at Mach 1.10, there is an increase in the pressure along both of the cylindrical and boattail parts due to the formation of the oblique shock waves.

B. Flow Over the Slotted-Wall Projectile

Passive cavity flow creates a good communication between upstream and downstream of the normal shock wave changing it into a weaker lambda shock structure. The following is a thorough discussion of the effect of streamwise slots on the flow over the projectile.

1. Effect of Suction/Blowing Mechanism

The suction/blowing mechanism in the case of streamwise slots is only confined to the area of the slot opening. Thus, limited viscous losses are incurred compared with the losses in the case of passive control by using porous surfaces [20]. Herein, the effect of streamwise slots is discussed over a range of Mach numbers to explain the suction/blowing mechanism in its on/off working mode.

Figure 11 illustrates the Mach contours around a projectile equipped with streamwise slots on its cylindrical and boattail parts. At Mach 0.85 and 0.90, there is no distinction between the contours around the slotted-walls projectile and their counterparts in the case of a solid-wall projectile shown in Fig. 9. This behavior is well supported by Fig. 10 where the pressure is almost constant along the cylindrical and boattail parts over the slotted-wall projectile. In this case, the mechanism of suction/blowing is switched off. At Mach

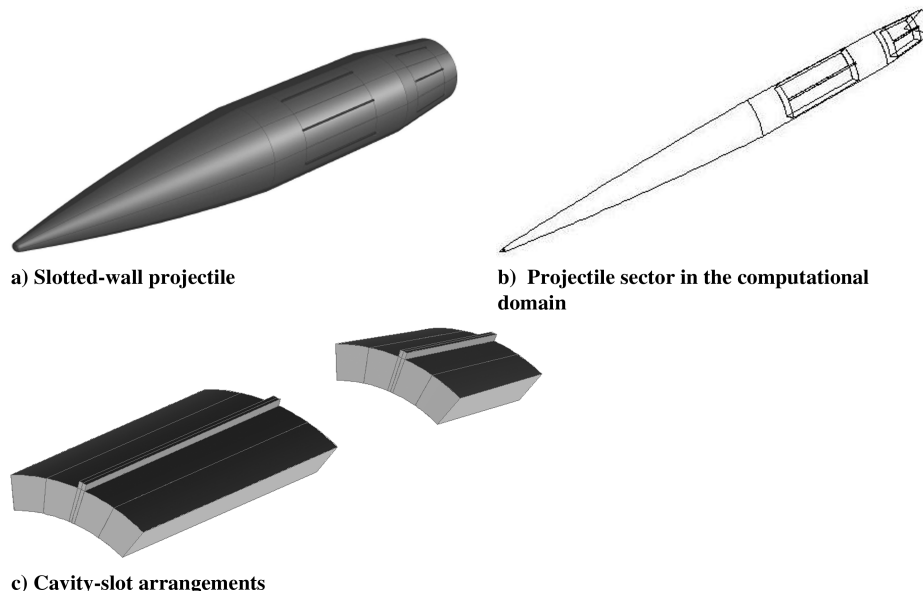


Fig. 5 Drawing of the slotted-wall projectile model.

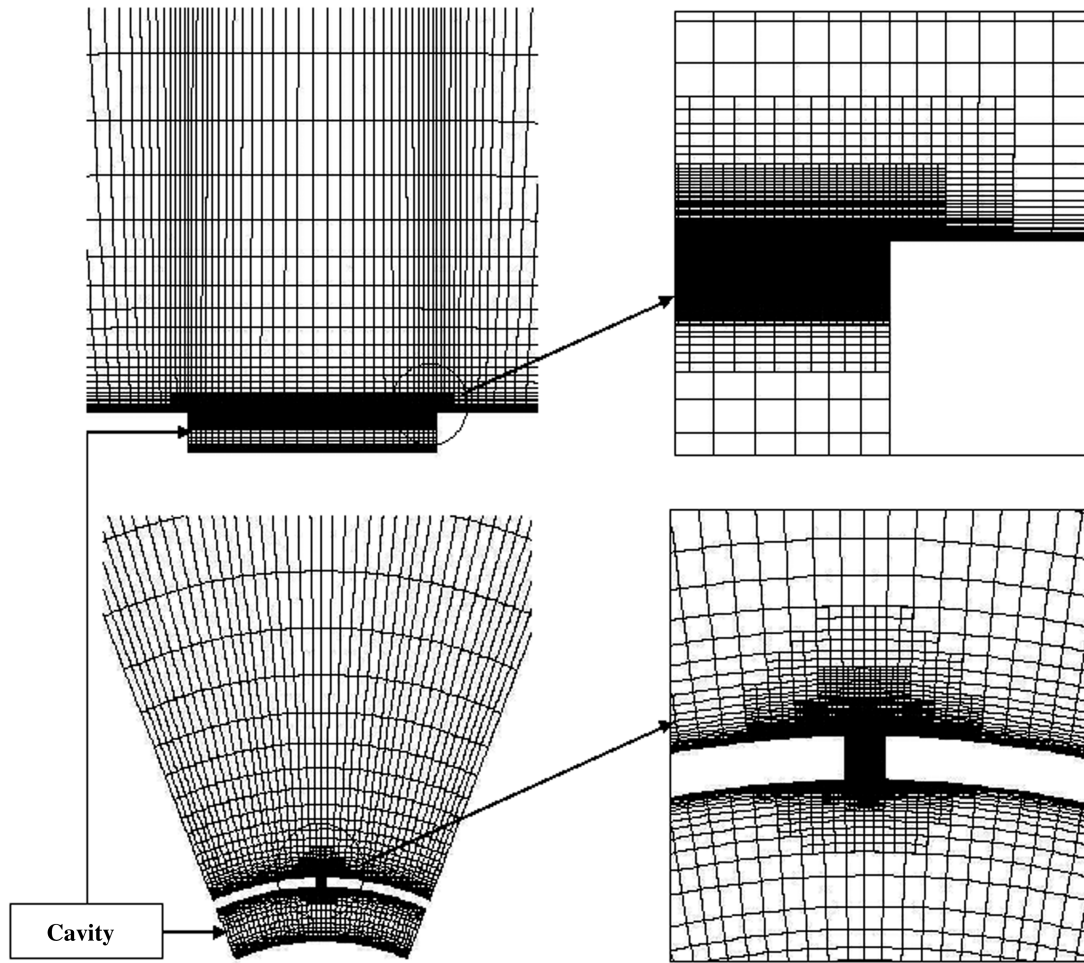


Fig. 6 Mesh refinement around the slot in both the axial and traverse directions.

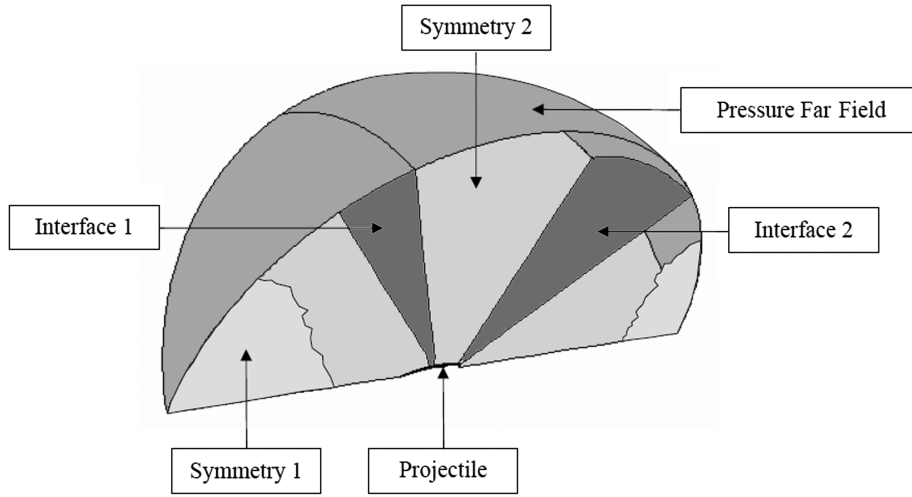


Fig. 7 Mesh boundary conditions.

0.96, the normal shock is transformed into a lambda shock structure resulting in a weaker interaction with the boundary layer. This means that the mechanism is switched on allowing recirculation of the flow through the cavity underneath the slots. At Mach 1.10, the flow pattern around the projectile is slightly changed. Because there is a weak adverse pressure gradient at this speed, the suction/blowing mechanism is switched on and the Mach contours get smeared.

While the normal shock waves transformed into lambda shock waves at Mach 0.96 and the Mach contours got smeared at higher speeds ($M = 1.10$), the streamwise slots look promising in reducing

the wave drag. However, according to the data recorded in Table 1, the reduction was insignificant.

The reasons of getting insignificant drag reduction can be figured out by comparing the effect of streamwise slots applied individually to either the cylindrical or the boattail parts at a Mach number of 0.96 with the baseline model. Figure 12 is a bar chart supported by a table comparing the total drag coefficient at each part of the projectile. The figure displays the projectile with three cases: solid-wall projectile, projectile with slotted cylinder, and another with a slotted boattail. In the case of the ogive part, the change in the drag coefficient in the

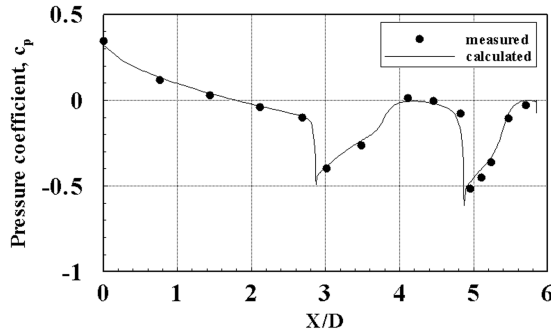


Fig. 8 Measured and calculated pressure coefficient past the solid projectile at $M = 0.96$.

three cases is negligible because this part has not been touched in this study.

First, let us compare the slotted-boattail projectile (columns with horizontal lines in the bar chart) with the solid one (black columns). Over the cylindrical part, there is no change in the drag force as long as the slots are applied to the boattail only. However, on the boattail part, a slight increase is noticed compared with the solid projectile. The drag rise is due to the viscous losses as the boundary layer is thickened over the slots. An interesting thing is noticed at the base drag which is the significant base drag reduction ($\Delta C_{db} = 22.5\%$ of the base drag in the case of the solid projectile). It is thought that the forming of the lambda shock wave over the boattail helps in getting higher base pressure. This pressure increase is due to the trailing leg of the lambda shock wave which represents a displacement of the original normal shock wave in the downstream direction. Figure 13 depicts distribution of the base pressure drag coefficient along the base radius normalized by the projectile caliber. An increase is noted in the base pressure in the case of the slotted-boattail projectile compared with the solid one.

Second, let us compare the slotted-cylinder projectile (columns with vertical lines) with the solid one (black columns). On the cylinder itself, a higher drag is noticed compared with the solid-wall cylinder. The values of the drag components showed an increase in

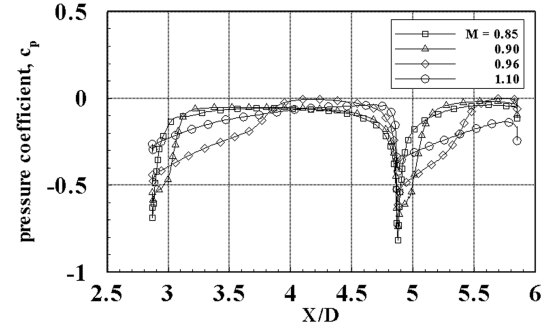


Fig. 10 Pressure coefficient over the solid cylindrical and boattail parts.

skin friction drag in the case of the slotted-wall cylinder. However, the base drag is slightly decreased due to the same reason discussed earlier in the case of the slotted-cylinder projectile. It is thought that the increase in viscous drag over the cylinder offsets this reduction in the base drag.

Hereafter, studying the flow physics over the slotted-wall projectile may help in finding some solutions for the streamwise slot device to get a beneficial effect on the drag reduction. Figure 14 displays the pressure coefficient along the solid and slotted cylindrical and boattail parts at a Mach number of 0.96. The pressure distribution for the controlled interaction shows the typical behavior of lambda shock wave structure. This shock can be detected from the pressure rise downstream of the leading and trailing edge legs, and the plateau in between.

Figure 15 illustrates the normal velocity distribution along a plane passing through the middle of the cylindrical and boattail slots. The normal velocity nearly vanishes on the cylindrical part at Mach numbers of 0.85 and 0.90, because there are no shock waves at these upstream speeds. However, a remarkable secondary flow is shown over the slot of the boattail part whatever the upstream speed. This is due to the geometrical nature of the boattail where the flow is changed due to the rapid expansion at the cylinder-boattail junction and due to the adverse pressure gradient [21]. Thus, the suction and

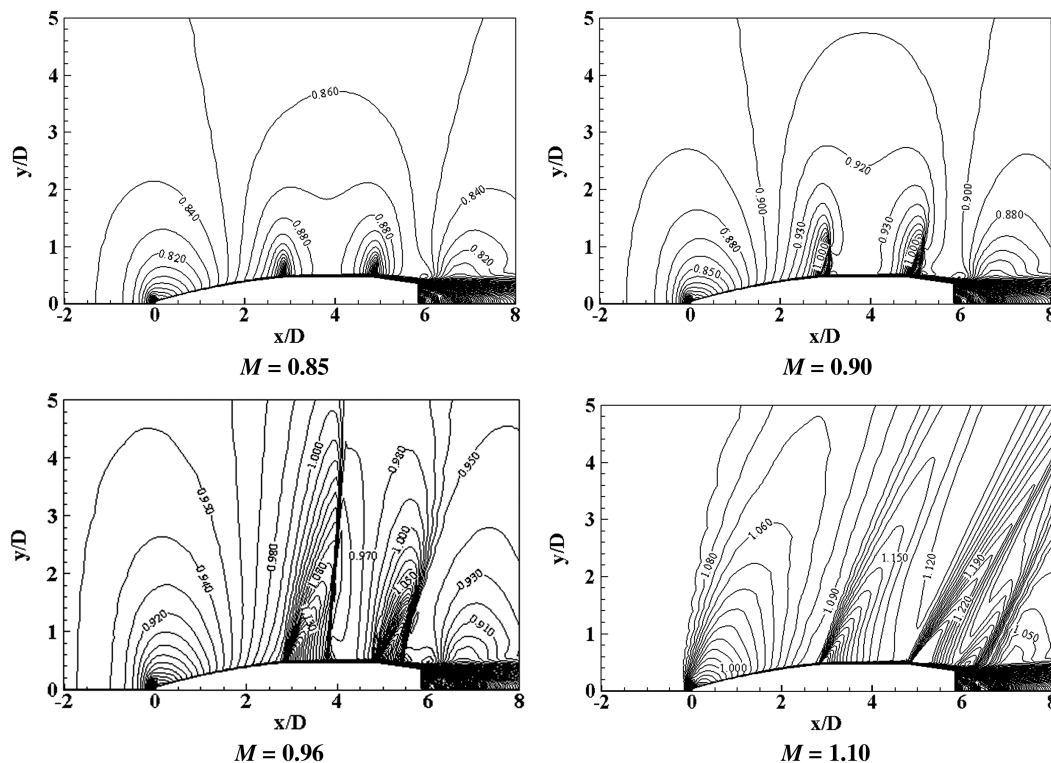


Fig. 9 Mach contours around the solid-wall projectile.

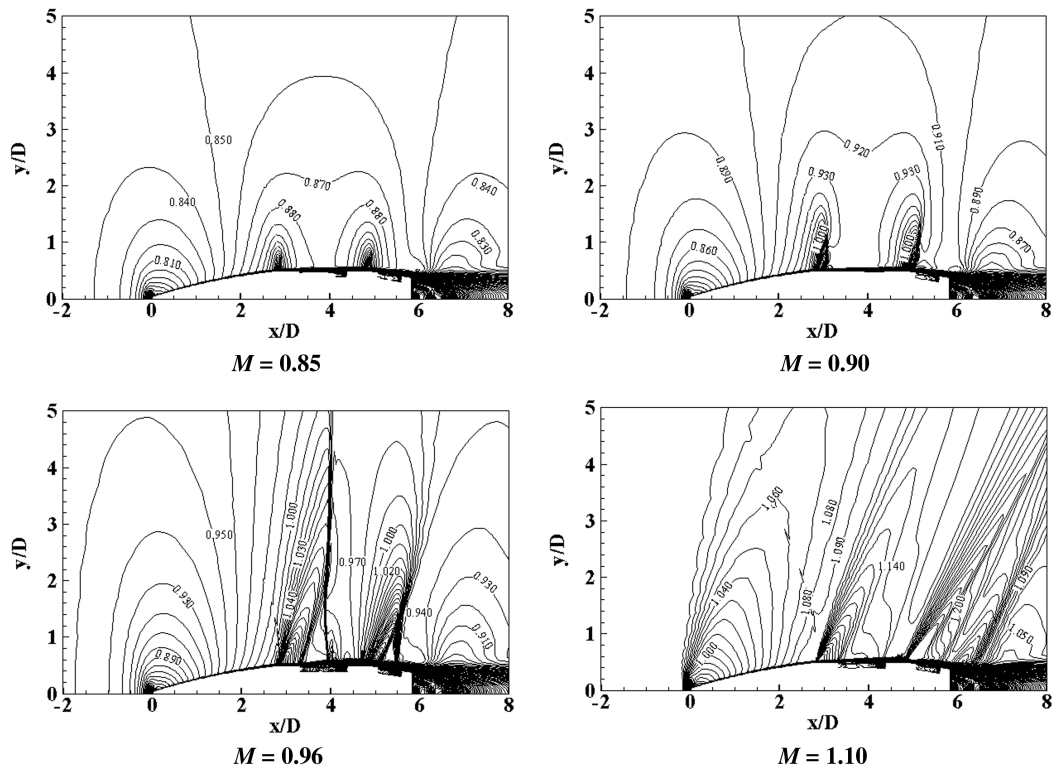


Fig. 11 Mach contours over the slotted-wall projectile.

blowing mechanism is always active on the boattail part. At Mach numbers of 0.96 and 1.10, the normal velocity distribution shows that the suction region is less than the blowing one with maximum suction and blowing strengths attained at Mach 0.96. Moreover, the extent of suction is inversely proportional to the strength of interaction. It is thought that the adverse pressure gradient is responsible for the difference in suction and blowing length. This can be explained by studying the mass flow rates through the slot in both suction and blowing regions. Comparing the secondary flow through the streamwise slots with that through a porous wall, the normal velocity distributions are similar. However, the maximum transpiration velocity by applying a porous surface should be less than 5.0% of the freestream velocity.

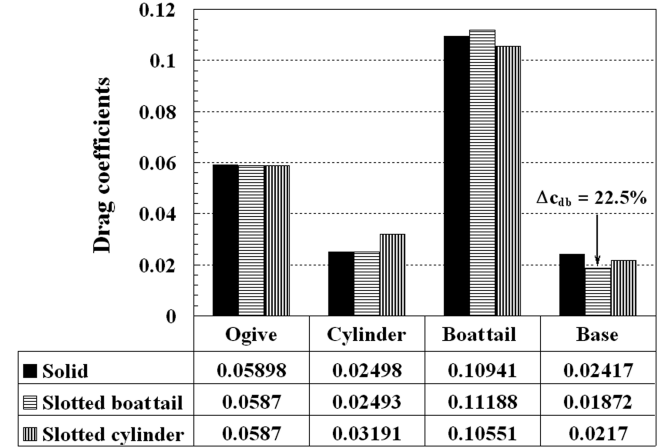
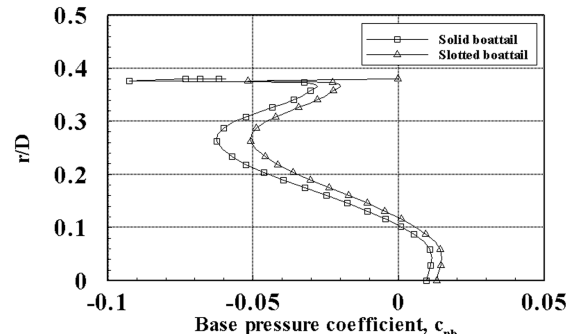
Figure 16 illustrates the pressure coefficient contours over the controlled surfaces. No particular feature is noticed at Mach numbers of 0.85 and 0.90 except some increase in the pressure over the boattail part due to its geometrical nature discussed earlier. At Mach 0.96, assuming that two air molecules started to move with the flow at the same time, one of them would move along a line passing at a slot side. The other one would move along a line on the middle between two slots. The former molecule will feel by the pressure rise first at the beginning of the blowing region. Going farther downstream, the molecule between the two slots feels the pressure rise first. This supports the suggestion of the three-dimensional shock wave structure that is mentioned by Smith et al. [20]. Finally, at Mach 1.10, low density of the pressure coefficient contours is noticed because the suction/blowing mechanism is weaker at this upstream speed compared with that at Mach 0.96.

Table 1 Drag components at different Mach numbers for solid and slotted-wall projectiles

M	Solid-wall projectile			Slotted-wall projectile		
	C_{dp}	C_{dsf}	C_D	C_{dp}	C_{dsf}	C_D
0.85	0.09339	0.06158	0.15497	0.09496	0.06060	0.15556
0.90	0.11635	0.06076	0.17711	0.11515	0.05953	0.17468
0.96	0.15649	0.06105	0.21754	0.15875	0.05760	0.21635
1.10	0.31713	0.06007	0.37720	0.31732	0.05838	0.37570

2. Effect of Streamwise Slots on the Boundary-Layer Profile

To understand the effect of streamwise slots on the boundary-layer profile, development of the boundary-layer velocity has been studied

Fig. 12 Comparison of the total drag coefficient at $M = 0.96$ for the solid, slotted-boattail, and slotted-cylinder projectiles.Fig. 13 Pressure coefficient on the projectile base at $M = 0.96$.

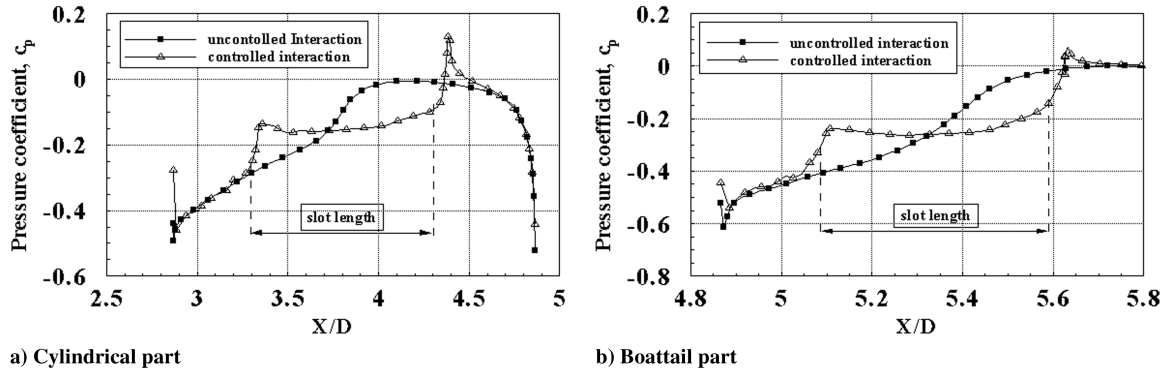
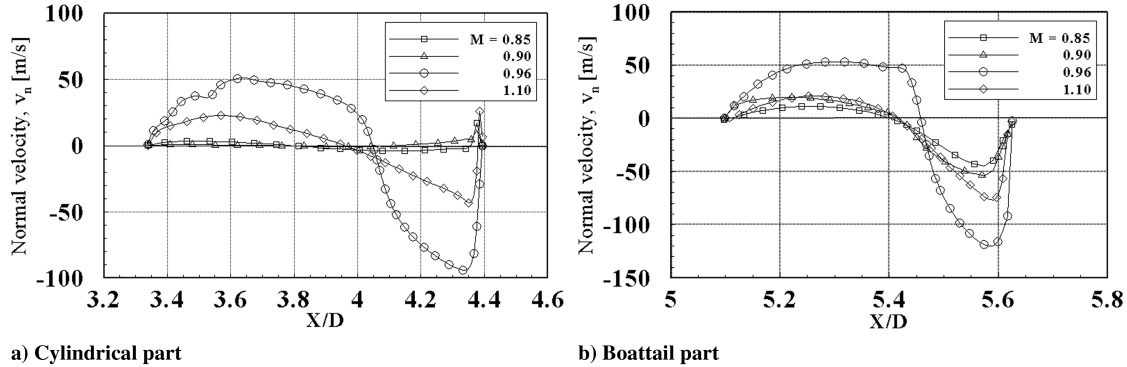
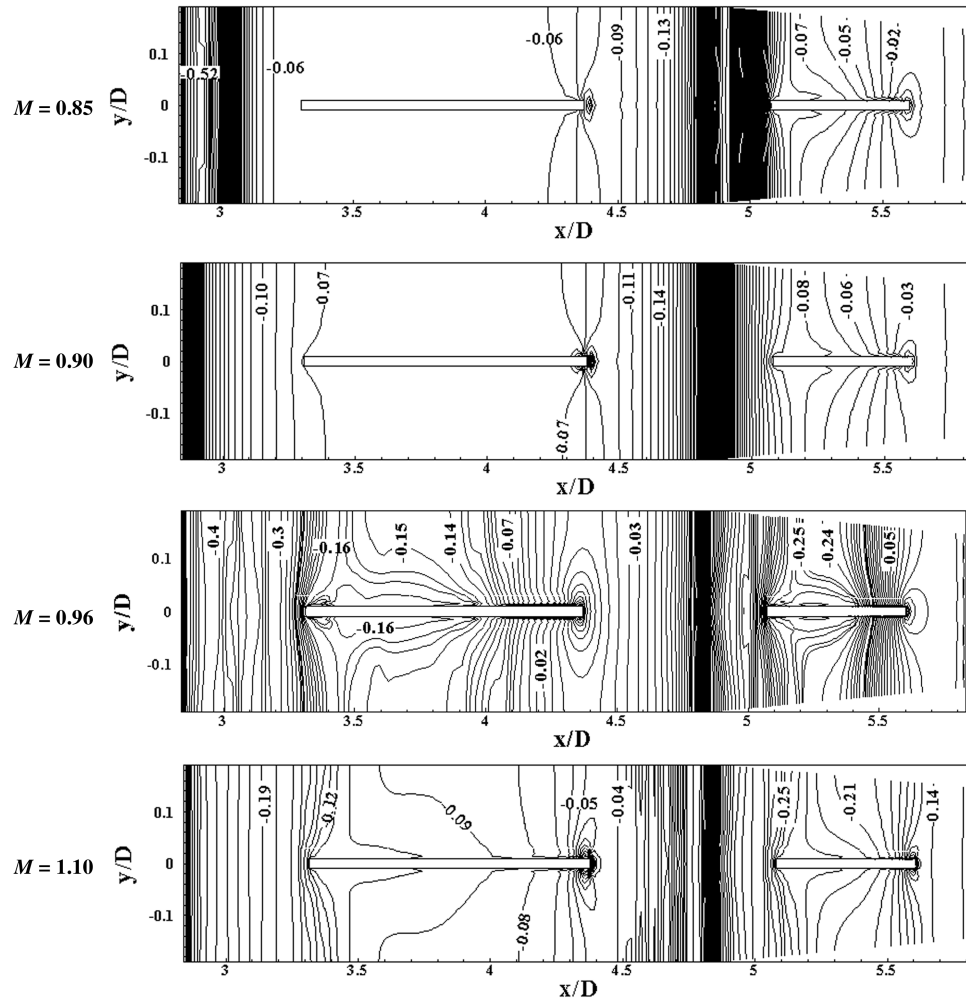
Fig. 14 Pressure coefficients for controlled and uncontrolled flow at $M = 0.96$.Fig. 15 Distribution of normal velocity distribution over a slot length at $M = 0.85–1.10$.

Fig. 16 Pressure coefficient contours over the controlled area.

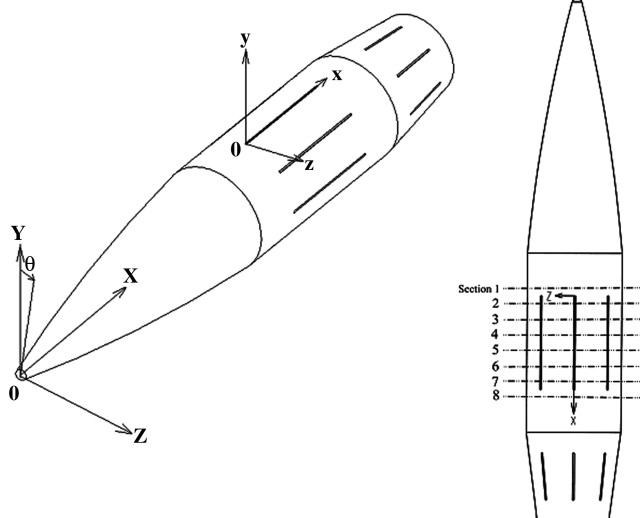


Fig. 17 Used system of coordinates and positions of the sections over the cylindrical part.

in both the streamwise and azimuth directions. For the streamwise direction, eight sections at 10.0 mm step were selected on the cylindrical part as shown in Fig. 17. The first section is located upstream of the slot at $x = -5.0$ mm with respect to the local coordinate system x , y , and z .

Figure 18 illustrates the boundary-layer velocity profiles along three longitudinal planes. The first is passing through the middle of the slot width (azimuth angle $\theta = 0.0$ deg), the second is along the mid-distance between two slots, and the third plane is along the baseline solid-wall projectile. The profiles of the boundary layer along the three planes are plotted against a lower abscissa normalized with a projectile caliber starting with $x/D = 0.0$. It can be seen that the boundary layer passing through the middle of the slot is thickened toward the downstream direction; this is caused by the effect of blowing. However, in the case of the controlled flow between two slots ($\theta = 22.5$ deg), the flow is similar to the uncontrolled interaction over a solid projectile.

Figure 19 shows the Mach contours across the same eight sections on the cylindrical part. At the first section, the boundary layer is homogenous around the solid part of the projectile circumference. At section 2, just downstream of the start of the slot, another profile of the Mach contours is noticed over the 1.0 mm slot width. There is some disturbance in the boundary layer over the slot opening due to the secondary flow from the cavity. The shape of this profile is going to the full boundary-layer profile on the solid wall, as the azimuth angle θ increases to the mid-distance between two slots. The next frames show enlargement of the boundary-layer profile over the region of the slot opening. Although section 8 is located downstream of the end of the slot, the behavior of the boundary-layer profile is still the same as those for the previous sections.

To study the development of the boundary-layer profile in the azimuth direction, the velocity profile is discussed at different azimuths angles ($\theta = 0.0, 4.5, 9.0, 13.5, 18.0$, and 22.5 deg).

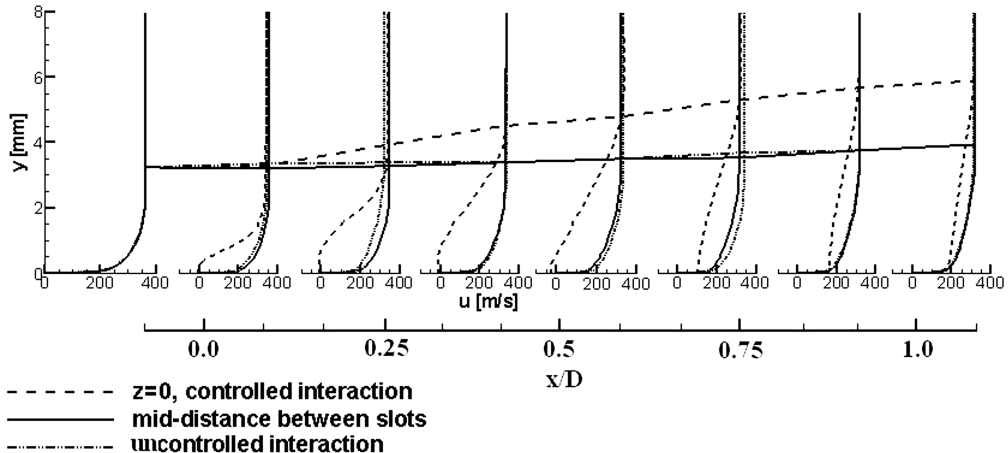


Fig. 18 Boundary-layer velocity profiles at cylindrical part sections.

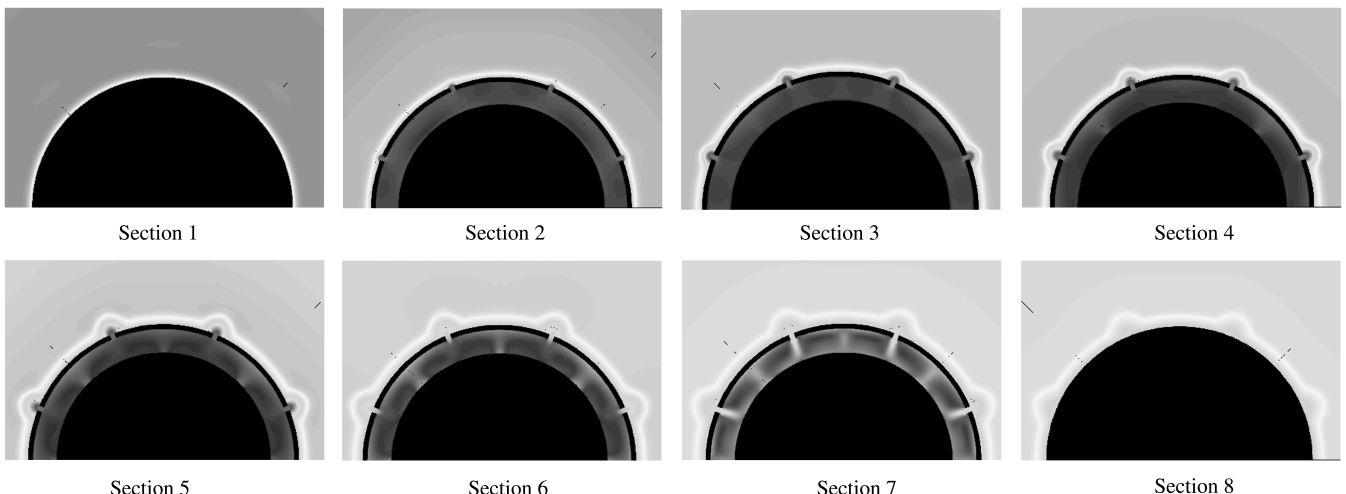


Fig. 19 Mach contours across cylindrical part sections.

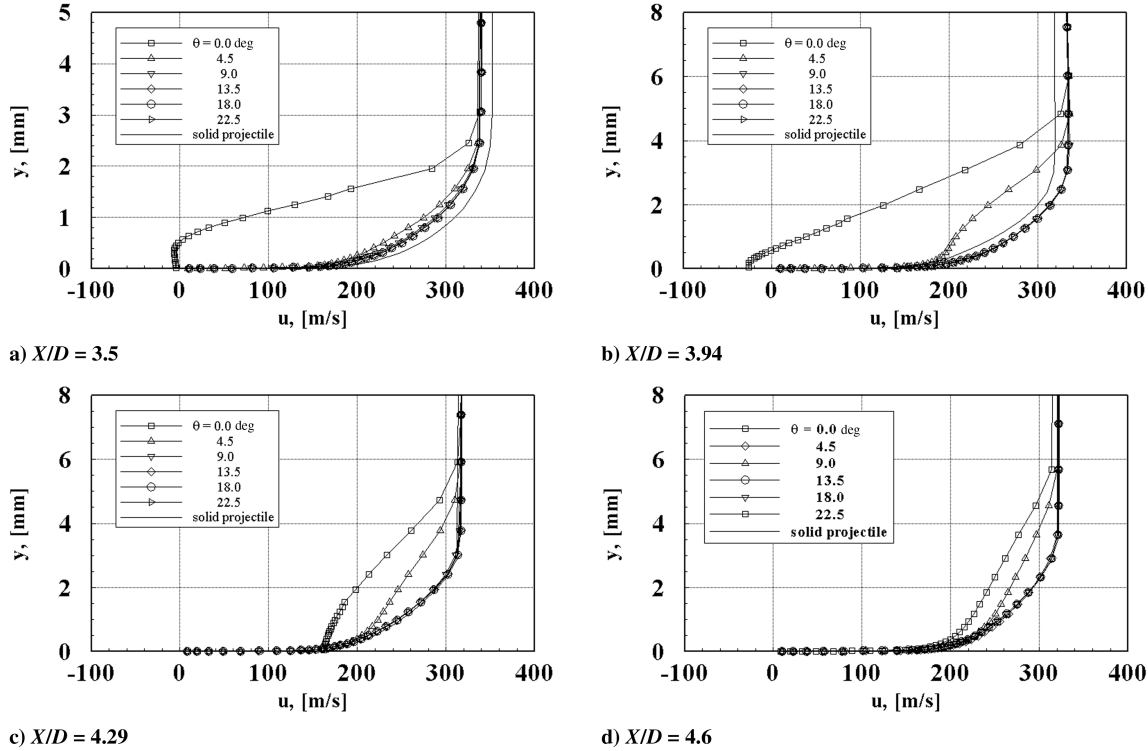
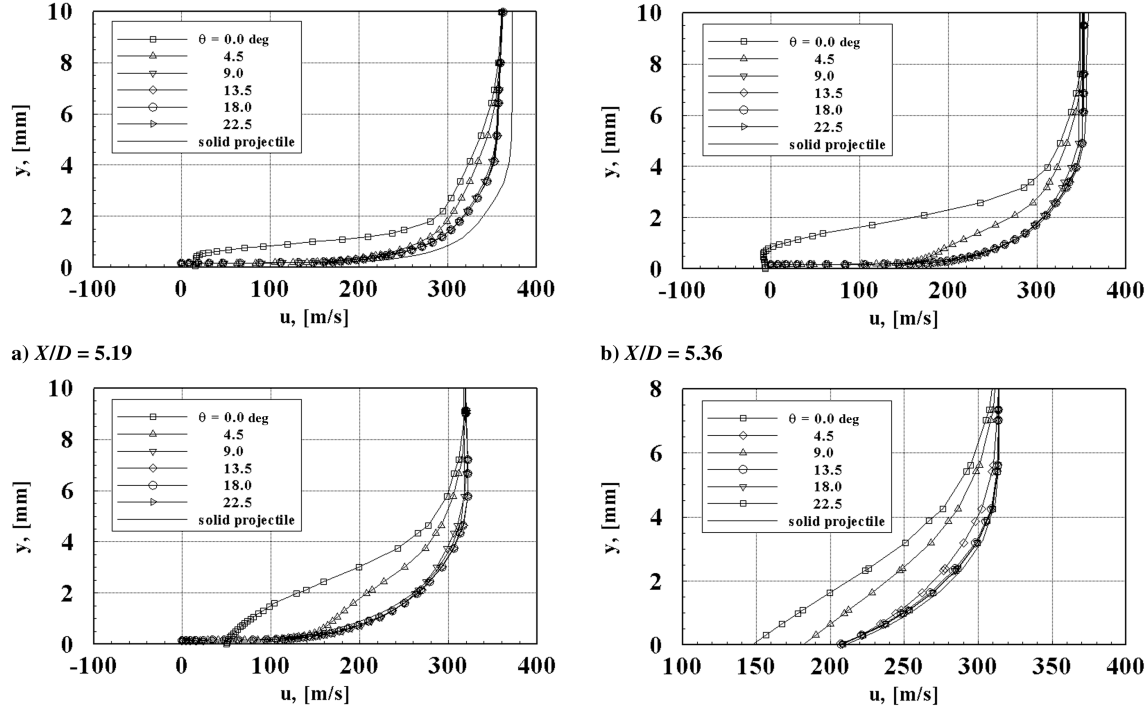
Fig. 20 Boundary-layer velocity profiles over the cylindrical part at $M = 0.96$.

Figure 20 displays the evolution of boundary-layer velocity profiles over four sections along the cylindrical part. The first three sections are located over the controlled area of interaction and the last one is located at the solid part downstream of the slot end. Figure 20a depicts the boundary-layer velocity profiles at the first section. The velocity profile at $\theta = 0.0$ deg is not full and a weak reverse flow can be noticed. The reverse flow is due to an axial component of blowing velocity because the streamwise slot does not confine the flow to be normal to the wall. This reverse flow vanishes quickly toward the

normal direction to the surface because the main flow velocity is considerably larger. As the azimuth angle increases, the boundary layer is going to the typical profile over an attached flow on the solid projectile.

In Fig. 20b, the boundary-layer velocity profile is still not full at $\theta = 0.0$ and 4.5 deg. Moreover, there is a remarkable reverse flow on the middle of the slot ($\theta = 0.0$ deg). The reverse flow disappears in the third section just before the end of the slot (as shown in Fig. 20c). However, the boundary layer is still thickened at $\theta = 0.0$ and 4.5 deg.

Fig. 21 Boundary-layer velocity profiles over the boattail part at $M = 0.96$.

The same trend is noted in Fig. 20d, although the flow is over a solid wall. The velocity profile has the typical development of the attached turbulent boundary layer but it is still thicker than its counterpart on the solid-wall projectile. From the previous discussion of Figs. 19 and 20, it can be concluded that the boundary layer is highly three dimensional which is in agreement with the suggestion mentioned in [20].

Figure 21 shows the evolution of boundary-layer velocity profiles over four sections along the boattail part at different azimuth angles. The first three sections are located on the slot, while the fourth is located on the solid part downstream of the slot end. A similar behavior to that of the boundary layer over the cylindrical part can be noted. Yet, the reverse flow is rather weak relative to that on the cylindrical sections. It is understood that the blowing velocity field

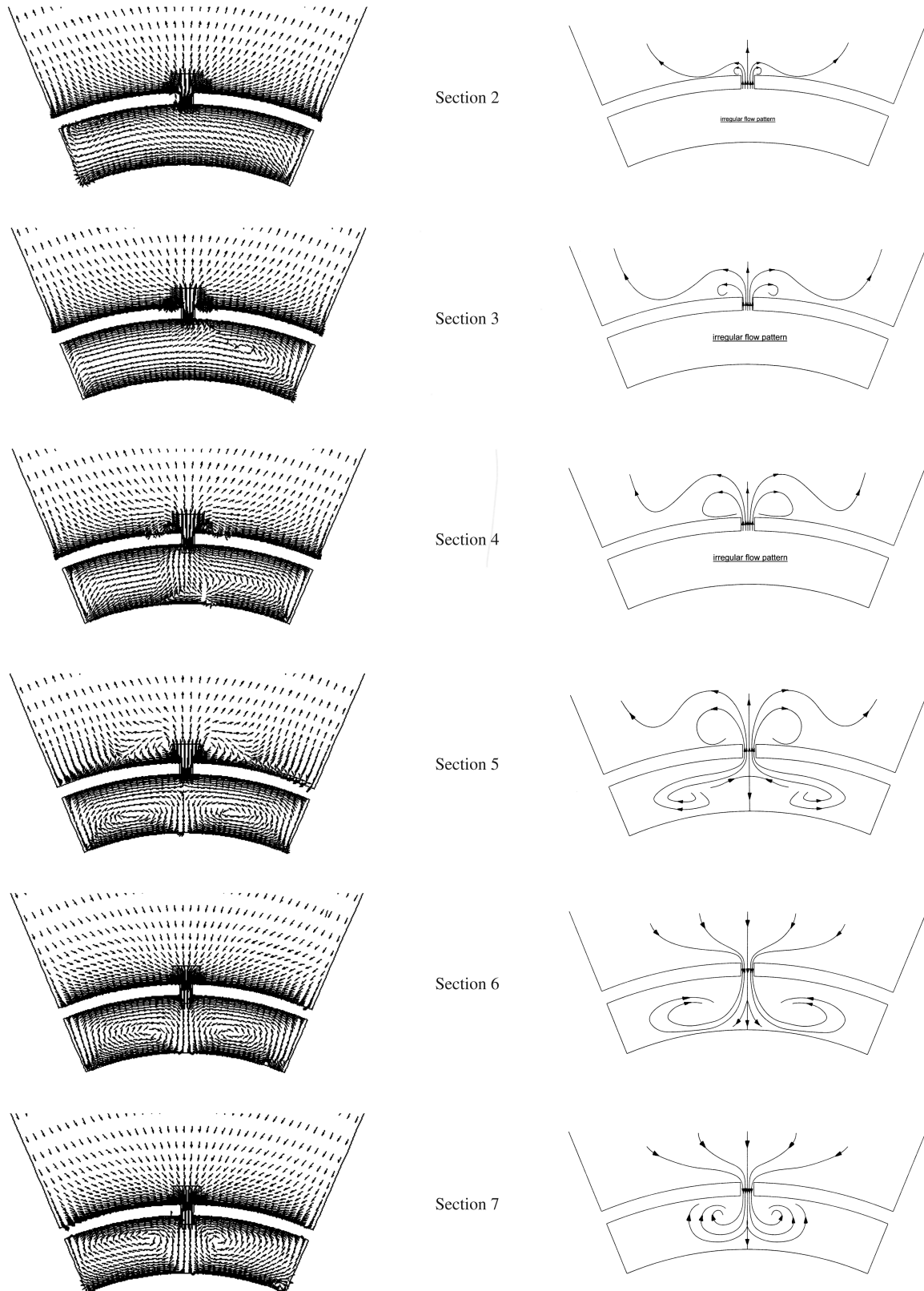


Fig. 22 Field of velocity vectors across the cylindrical slot sections.

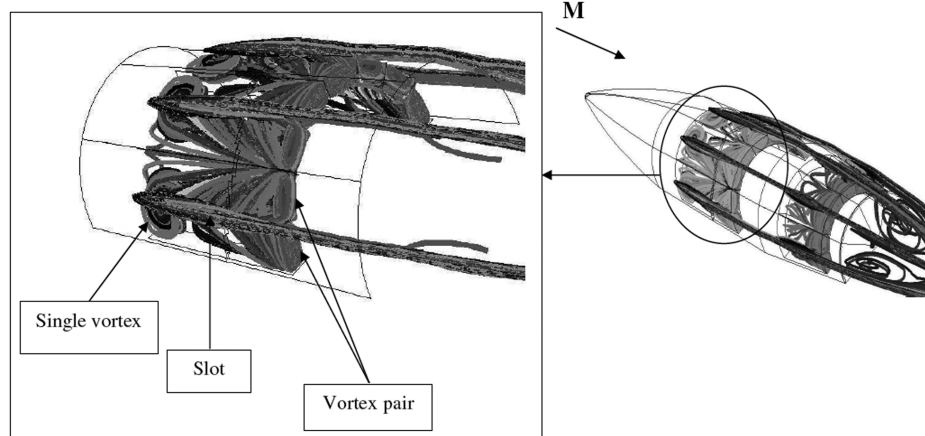


Fig. 23 Flow tracking inside the cylindrical cavity at $M = 0.96$.

will have a decrease of its inclination angle equal to the boattail angle ($\beta = 7.0$ deg) resulting in decreasing the reverse flow.

3. Flow Pattern Around the Projectile with Streamwise Slots

The flow pattern in the slot-cavity arrangement was studied by displaying the field of velocity vectors on six sections selected across the cylindrical slot (sections 2–7 in Fig. 17). Sections 2–5 are located on the blowing region, while the last two sections are located on the suction region. Figure 22 displays the field of velocity vectors on these sections as well as sketches explaining the corresponding velocity field pattern. The pattern of the flowfield at section 2 shows the formation of an opposite-circulation vortex pair (OVP) formed as the flow leaves the slot. This OVP grows with the downstream direction as shown in sections 2–5. In the suction regions, at sections 6 and 7, no vortices are noted, while the flow enters the slot. This means that the OVP is not extended to the whole slot length; it is extended along the blowing region only.

The study of the development of the flow pattern inside the cavity starts from its upstream direction (suction region) toward the downstream direction (blowing region). Thus, starting from section 7, the formation of OVP is noted. This OVP is due to the impact of the incoming flow with the bottom wall of the cavity. The result is a splitting of the flow into two counter vortex pairs. The OVP grows toward the downstream direction of the cavity flow and extends up to the borders between the suction and blowing regions. This can be seen from the sketches of flow patterns starting from section 7 up to 5. For the sections 4 up to 2, no regular patterns have been found for the flow inside the cavity. It was thought that there is something wrong with the displaying of velocity vectors. The flow mechanism was clarified by displaying the path lines of the flow inside the cavity, as shown in Fig. 23. While the OVP discussed earlier can be noted inside the cavity under the suction region, a single vortex perpendicular to the cavity flow is formed under the blowing region. This vortex has the shape of a conical helix with a base attached to the cavity floor. The formation of this vortex is the way to turn the flow from the horizontal direction to the vertical direction in order to leave the narrow slot opening. Investigation of the bulk flow direction inside the cavity at sections 2 and 3 gives another indication of the single vortex formation, because both have opposite bulk flow directions. Therefore, it is thought that this vortex is responsible for the irregularity of the velocity field inside the cavity at sections 2–4. The pattern of the flow inside the cavity of the boattail showed a formation of OVP as discussed in the case of the cylindrical one but the single vortex is rather weak.

Figure 24 depicts the distribution of the normal velocity over both the cylindrical and the boattail slots. It can be noted that there is a drop in the normal velocity on the blowing region of the cylindrical slot. It is thought that this drop is corresponding to the single vortex axis. For the boattail, the vortex was relatively weak resulting in smooth distribution of the normal velocity over the blowing region.

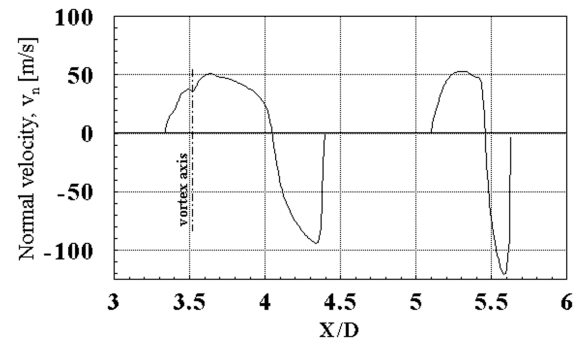


Fig. 24 Normal velocity distribution at $M = 0.96$.

IV. Conclusions

A computational study has been performed to investigate the effect of streamwise slots on an SOCBT projectile. The results showed the effectiveness of the suction/blowing mechanism through the slot at transonic speeds. The study of the boundary-layer velocity profiles and flow pattern at Mach 0.96 was thoroughly investigated. The suction region was found to be shorter than the blowing one for the present case in which the slot width is constant. The drag was not affected significantly by applying the pattern of streamwise slots as discussed in this paper. A reverse flow area was detected in the boundary-layer velocity profiles at the blowing region. It is thought that this reverse flow can be reduced by using conventional methods of passive control over the blowing region. Thus, the combination of the streamwise slots over the suction region and porous wall over the blowing region may be beneficial. A formation of a single vortex inside the cavity in the blowing region has been detected. It is thought that preventing the formation of this vortex using the porous wall will decrease the blowing velocity resulting in a reduction of viscous losses. Based on the present results, it is recommended to do a parametric study investigating the number of slots and their geometrical shape. This study may help in knowing to what extent the streamwise slots affect the drag reduction.

References

- [1] Tanner, M., "Reduction of Base Drag," *Progress in Aerospace Sciences*, Vol. 16, No. 4, 1975, pp. 369–384.
- [2] Platou, A. S., "Improved Projectile Boat-Tail," *Journal of Spacecraft and Rockets*, Vol. 12, No. 12, 1975, pp. 727–732.
- [3] Liang, S., and Fu, J., "Passive Control Method for Drag Reduction for Transonic Projects," AIAA Paper 91-3213-CP, 1991.
- [4] Fu, J., and Liang, S., "Drag Reduction for Turbulent Flow over a Projectile: Part 1," *Journal of Spacecraft and Rockets*, Vol. 31, No. 1, 1994, pp. 85–92.
- [5] Liang, S., and Fu, J., "Drag Reduction for Turbulent Flow over a Projectile: Part 2," *Journal of Spacecraft and Rockets*, Vol. 31, No. 1, 1994, pp. 93–98.

- [6] Bahi, L., Ross, J. M., and Nagamatsu, H. T., "Passive Shock Wave/Boundary-Layer Control for Transonic Airfoil Drag Reduction," AIAA Paper 83-0137, 1983.
- [7] Nagamatsu, H. T., Orozco, R. D., and Liang, D. C., "Porosity Effect on Supercritical Airfoil Drag Reduction by Shock Wave/Boundary-Layer Control," AIAA Paper 84-1682, 1984.
- [8] Savu, G., and Trifu, O., "Porous Airfoils in Transonic Flow," *AIAA Journal*, Vol. 26, No. 7, 1984, pp. 989-991.
- [9] Chen, C., Chow, C., Holst, T., and Van Dalsem, W., "Numerical Simulation of Transonic Flow over Porous Airfoils," AIAA Paper 85/5022, 1985.
- [10] Nagamatsu, H. T., Dyer, R., and Ficarra, R. V., "Supercritical Airfoil Drag Reduction by Passive Shock/Boundary-Layer Control in the Mach Number Range 0.75 to 0.90," AIAA Paper 85-0207, 1985.
- [11] Hartwich, P. M., "Euler Study on Porous Transonic Airfoils with a View Toward Multipoint Design," AIAA Paper 91/3286, 1991.
- [12] Mineck, R. E., and Hartwich, P. M., "Effect of Full-Chord Porosity on Aerodynamic Characteristics of the NACA 0012 Airfoil," NASA Technical Paper 3591, 1996.
- [13] Hsiung, J., and Chow, C., "Drag Reduction of Transonic Projectile by Porous Surface," AIAA Paper 93/0417, 1993.
- [14] Hsiung, J., and Chow, C., "Computed Drag Reduction on a Projectile Using Porous Surfaces," *Journal of Spacecraft and Rockets*, Vol. 32, No. 3, 1995, pp. 450-455.
- [15] Ibrahim, A., and Filippone, A., "Effect of Porosity Strength on the Drag Reduction of a Transonic Projectile," *Journal of Aircraft*, Vol. 44, No. 1, 2007, pp. 310-316.
- [16] Raghunathan, S., "Passive Control of Shock-Boundary Layer Interaction," *Progress in Aerospace Sciences*, Vol. 25, No. 3, 1988, pp. 271-296.
- [17] Chen, C., Chow, C., Van Dalsem, W., and Holst, T., "Computation of Viscous Transonic Flow over Porous Airfoils," *Journal of Aircraft*, Vol. 26, No. 12, 1989, pp. 1067-1075.
- [18] Smith, A. N., Babinsky, H., Fulker, J. L., and Ashill, P. R., "Experimental Investigation of Transonic Aerofoil Shock/Boundary-Layer Interaction Control Using Streamwise Slots," *Proceedings of the IUTAM Symposium*, Goettingen, Germany, 2002, pp. 285-290.
- [19] Spalart, P. R., and Allmaras, S. R., "A One-Equation Turbulence Model for Aerodynamic Flows," AIAA Paper 92-0439, 1992.
- [20] Smith, A. N., Babinsky, H., Fulker, J. L., and Ashill, P. R., "Shock-Wave/Boundary-Layer Interaction Control Using Streamwise Slots in Transonic Flows," *Journal of Aircraft*, Vol. 41, No. 3, 2004, pp. 540-546.
- [21] Herrin, J. L., and Dutton, J. C., "Supersonic Near-Wake Afterbody Boat-Tailing Effects on Axisymmetric Bodies," *Journal of Spacecraft and Rockets*, Vol. 31, No. 6, 1994, pp. 1021-1028.